

Thermal Temperature Measurements of Inertial Fusion Implosions

L. C. Jarrott,* B. Bachmann, T. Ma, L. R. Benedetti, F. E. Field, E. P. Hartouni, R. Hatarik, N. Izumi, S. F. Khan, O. L. Landen, S. R. Nagel, R. Nora, A. Pak, J. L. Peterson, M. B. Schneider, P. T. Springer, and P. K. Patel
Lawrence Livermore National Laboratory, Livermore, California 94550, USA

 (Received 20 April 2018; revised manuscript received 14 May 2018; published 22 August 2018)

Accurate measurement of the thermal temperature in inertially confined fusion plasmas is essential for characterizing ignition performance and validating the basic physics understanding of the stagnation conditions. We present experimental results from cryogenic deuterium-tritium implosions on the National Ignition Facility using a differential filter spectrometer designed to measure the thermal electron temperature from x-ray continuum emission from the stagnated plasma. Furthermore, electron temperature measurements, used in conjunction with the Doppler-broadened DT neutron spectra, allow one to infer the partition of energy in the hot spot between internal energy and unconverted kinetic energy.

DOI: [10.1103/PhysRevLett.121.085001](https://doi.org/10.1103/PhysRevLett.121.085001)

Inertial confinement fusion (ICF) experiments at the National Ignition Facility (NIF) seek to implode a spherical capsule made of cryogenic deuterium-tritium (DT) ice surrounding gaseous DT [1–5], producing a controlled thermonuclear burn of the DT fuel. Primary measurables which characterize the performance of these ICF reactions include the total fuel areal density (ρR) and the ion temperature (T_i) of the central DT “hot spot.” Together, these quantities can be used to form a modified Lawson criterion [6] of the form $(\rho R)_{\text{no-}\alpha}^{0.8} T_{\text{no-}\alpha}^2 > 1$ derived in Ref. [7], where the ρR term is normalized to 1 g/cm² and the hot-spot temperature is normalized to 4.3 keV. The high-foot campaign on the NIF produced the first implosions to achieve significant levels of alpha-particle self-heating, but, as reported by Hurricane *et al.* [8], a major anomaly of these experiments was the inference of DT ion temperatures exceeding 5.5 keV, values far higher than expected from the theory or simulation. Additionally, measured ion temperatures from DT reactions and deuterium-deuterium (DD) reactions reported temperature differences (>1 keV) inconsistent [9–11] and unphysical [8,12] with our current understanding of the individual reactivities.

Several hypotheses exist which could individually [12] or collectively [9] explain this discrepancy and can be categorized into two scenarios. The first involves hypotheses that would explain why the temperature is, in fact, higher than expected. The second involves hypotheses in which the temperature is actually lower than what is being measured. In the first scenario, having a reduced thermal conductivity within the hot spot, e.g., would increase the necessary temperature for a given neutron yield [12]. Or, kinetics effects, such as shock-induced ion species separation within the hot spot, would similarly increase the necessary temperature for a given neutron yield [13]. For the second scenario, one of the leading hypotheses is *fluid velocity flows* artificially

enhancing the inferred temperature from neutron spectroscopy diagnostics. Current ICF experiments measure the ion temperature using neutron time-of-flight (NTOF) detectors, which measure the velocity variance of the DT neutron spectral peak produced within the imploded target that subsequently reaches the detector. Implicitly coupled with a velocity-variance measurement using this time-of-flight spectroscopy are “bulk” fluid velocities, indistinguishable from velocities due to internal energy. More specifically, the kinetic energy of a neutron produced from a DT reaction will contain information about the center-of-mass (c.m.) velocity of the deuterium and tritium reactants regardless of the form and origin of the particular reactant’s velocity in the fusing plasma. This nonthermal velocity component has been previously [9–11] referred to as residual kinetic energy (RKE), which can arise from low-mode asymmetries in the implosion, resulting in an incomplete conversion of fuel kinetic energy to internal energy during stagnation. A measurement of the true thermal temperature of the hot spot is then critical for differentiating between these competing hypotheses and for providing a better understanding of the stagnation conditions, degradation mechanisms, and proximity to ignition.

In this Letter, we present the first thermal temperature measurements of the hot spot in a series of cryogenic DT implosions on the NIF based on the observed x-ray bremsstrahlung emission spectrum which are sufficiently accurate to distinguish from current neutron-weighted ion temperature measurements. The x-ray spectrum depends on the internal energy of the hot spot electrons, or temperature, and is not influenced by residual velocity flow within the hot spot. We show that the x-ray inferred electron temperature is closely related to, and can be used to infer, the neutron-averaged thermal ion temperature. This, in turn, enables us to isolate the residual flow velocity term in the NTOF velocity variance measurement.

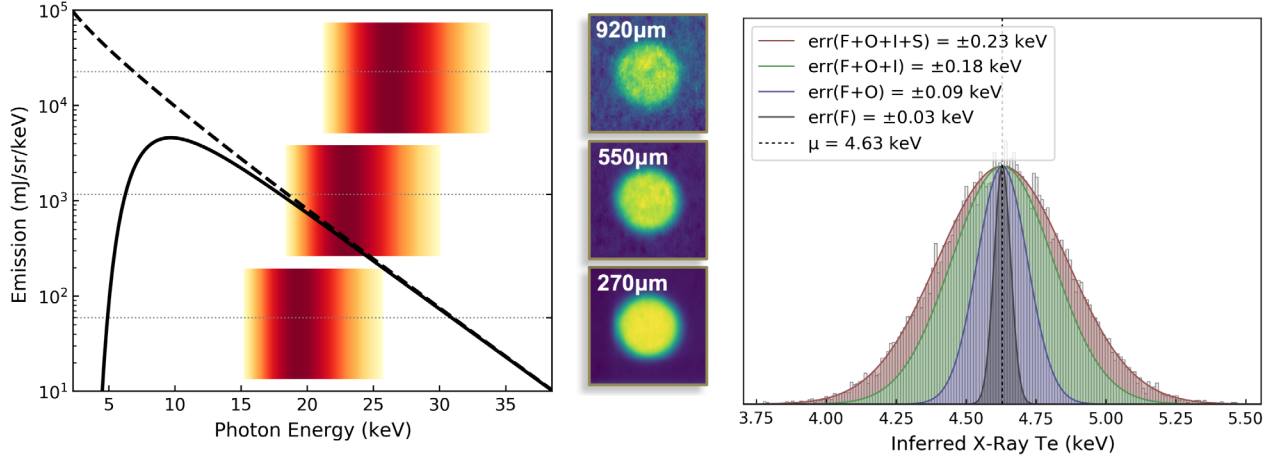


FIG. 1. Titanium differential filter spectrometer diagnostic layout. (Left) Bremsstrahlung x-ray emission from the hot spot at a characteristic temperature, leaves the hot spot (dotted black line) and is attenuated by the fuel shell and remaining ablator (solid black line). It then passes through the differential filters of 270, 550, and 920 μm , with each filter allowing a different mean x-ray energy to pass through as shown by the normalized sensitivity. (Middle) The x-ray signal from each filter is then deposited onto IP film. The IP signal from each filter is then used to reconstruct the x-ray emission spectra escaping the hot spot and passing through the fuel shell and ablator. (Right) Monte Carlo analysis of a particular cryogenic experiment on the NIF using uncertainties associated with filter thickness $\text{err}(F)$, optical depth $\text{err}(O)$, IP spectral response $\text{err}(I)$, and signal error $\text{err}(S)$ are sequentially added in quadrature and used to create a distribution of best-fit inferred x-ray electron temperatures.

X-ray continuum measurements were made with a new diagnostic, the titanium differential filter spectrometer (TiDFS), as shown in Fig. 1. Here, bremsstrahlung emission (per unit volume and time) is produced within the hot spot, parametrized with a characteristic temperature (T_e) and shell optical depth τ , according to the following equation:

$$\chi(\nu, T_e) = 4\pi \frac{\rho_{\text{DT}}^2 A_e^2}{\bar{A}^2} \frac{e^{-h\nu/T_e} e^{-\tau_\nu}}{(h\nu)^{0.39} T_e^{0.15}}. \quad (1)$$

This x-ray emission then escapes the hot spot and is attenuated by the fuel and remaining ablator, parametrized here using an $h\nu^3$ scaling of x-ray attenuation for an optical depth τ , evaluated at a photon energy of 10.85 keV. This results in a system with two degrees of freedom, which can be explicitly characterized using three filter thicknesses. As can be seen in Fig. 1, titanium filters were chosen with thicknesses of 270, 550, and 920 μm . When the hot-spot x rays pass through the filters, the distribution of photons transmitting through each is modified, with thicker filters having a higher mean photon energy than thinner filters. The normalized sensitivities for each filter can be seen in Fig. 1 plotted along with a bremsstrahlung emission spectrum from a 5 keV hot spot without shell attenuation (dashed line) and with a fuel-ablator optical depth of $\tau(@10.85 \text{ keV}) = 0.5$ (solid line). The x rays passing through each filter are then deposited onto spectrally calibrated image plate (IP) film [14,15]. With these three different photon distributions recorded by the IP, the original distribution of x rays escaping the fuel shell can be uniquely determined within the measurement accuracy of the diagnostic. In order to

minimize measurement uncertainty, the TiDFS utilizes a series of design choices which optimize measurement precision and minimize model dependency and can be found in more detail in Ref. [16]. Briefly, collimators have been used in place of pinholes, 140 μm in diameter, larger than the $\sim 60 \mu\text{m}$ hot-spot diameter improving the statistical error of the data while allowing for thicker filtration for a given minimum required spectral fluence.

Primary sources of measurement uncertainty come from signal to noise, filter thickness uncertainty, IP spectral sensitivity, and optical depth uncertainties. These measurement uncertainties are evaluated using a Monte Carlo approach applied to each source of error from experimental data allowing for correct error propagation using nontrivial error probability distribution functions. The results of this characterization can be seen in Fig. 1(c), represented as normal fits to histograms of the variance in the inferred electron temperature, where each source of error has been iteratively added to the total error beginning with the filter thickness error $\text{err}(F) \sim \pm 30 \text{ eV}$, followed by a quadrature sum of the filter and optical depth error $\text{err}(F + O) \sim \pm 90 \text{ eV}$, and then a quadrature sum including the IP error $\text{err}(F + O + I) \sim \pm 190 \text{ eV}$, and, finally, the x-ray signal error $\text{err}(F + O + I + S) \sim \pm 240 \text{ eV}$, with a best-fit temperature for this particular experiment of 4.6 keV. This error analysis has also been carried out for a series of cryogenic DT experiments showing error bars in a range of 5%–12%. The analysis in Fig. 1(c) is from a recent “repeat” of a previous high-foot, high-gas fill cryogenic DT implosion on the NIF where ion temperatures were consistently higher than model-predicted neutron yield scaling with the ion temperature [8]. The electron temperature for this particular

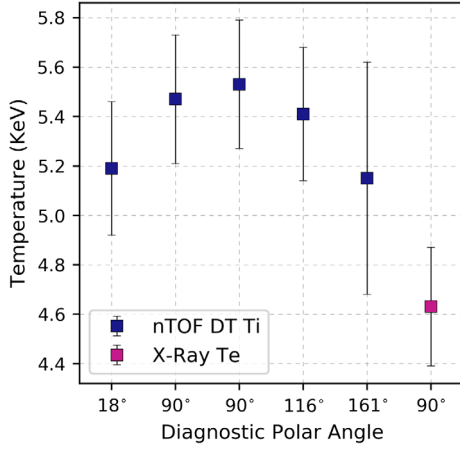


FIG. 2. Ion and electron temperature measurements from a recent cryogenic DT implosion on NIF. The bottom axis shows the polar viewing angle for each diagnostic. All five NTOF diagnostics infer a higher hot-spot temperature compared to the x-ray electron temperature measurement by as much as 900 eV, similar to previous speculation of the temperature overprediction.

experiment is plotted in Fig. 2 along with DT ion temperature measurements from five NTOF detectors. In this comparison, the electron temperature is systematically lower than all five DT ion temperature measurements. It is important to appreciate, however, that these are two measurements of two different physical quantities and might not necessarily agree. The two temperatures may differ for two reasons, regardless of residual velocity flows: first, *species* temperature differences between electrons and ions not in equilibrium and, second, measurement *weighting* differences, because the two measurements are integrated over a plasma temperature distribution with spatial and temporal variation and have implicit differences in their temperature sensitivities. The first of these could be present due to the fact that early in the implosion, shocks preferentially heat the ions, while later in the implosion, alpha particles preferentially heat the electrons. The electron-ion equilibration rate will determine the extent to which these two species are driven into thermal equilibrium with each other.

Temperature weighting differences can be understood by examining the scaling differences of each measurement within a nominally assembled hot spot. For DT reactions, the neutron production rate, within the temperature range of NIF DT implosions, scales with $T_i^{4.7}$ from Ref. [6], whereas the x-ray emissivity scales as e^{-E/T_e} and therefore depends on the particular photon energies being detected, with higher photon energies preferentially weighting towards hotter temperatures within the hot spot. In the case of a perfectly isothermal hot spot, the two measurements would be identical. One can estimate the relationship between a neutron-weighted (T_i^{NW}) and emissivity-weighted (T_e^{EW}) temperature measurement, assuming thermal

equilibrium of species ($T_e = T_i$), using a simple isobaric model of the hot spot, with a radial temperature profile given by [6]

$$T^{HS}(r) = T_0^{HS} \frac{[1 - (\frac{r}{R_0})^2]^{2/5}}{[1 - 0.15(\frac{r}{R_0})^2]}, \quad (2)$$

where T_0^{HS} and R_0 are the peak temperature and maximum radius of the hot spot, respectively. The neutron-weighted temperature can be calculated using the following equation for the DT neutron yield (per unit volume and time) as a function of the temperature:

$$Y_{DT}(r) = f_D f_T \frac{A_v^2}{A^2} \rho_{DT}^2 \langle \sigma_{DT} v(T_i) \rangle. \quad (3)$$

The average neutron-weighted temperature T_i^{NW} for a given peak hot-spot temperature is then

$$T_i^{NW}(T_0^{HS}) = \frac{\int_0^{R_0} Y_{DT}(r) T^{HS}(r) 4\pi r^2 dr}{\int_0^{R_0} Y_{DT}(r) 4\pi r^2 dr}. \quad (4)$$

To solve for an emissivity-weighted hot-spot temperature, we use Eq. (1), integrated over the hot spot:

$$\chi^{HS}(\nu, T_0^{HS}) = \frac{1}{(4/3)\pi R_0^3} \int_0^{R_0} \frac{\rho^2(r) e^{-h\nu/T^{HS}(r)}}{[h\nu]^{0.39} [T^{HS}(r)]^{0.15}} 4\pi r^2 dr. \quad (5)$$

This multitemperature hot-spot emissivity function can then be used to infer a single, emissivity-weighted temperature by taking its derivative. But, this inferred “single” temperature will change depending on what photon energies it is being evaluated at. We therefore evaluate the derivative of Eq. (5) at the mean sensitivity of the TiDFS ($h\nu = 20$ keV) as follows:

$$\left. \frac{\partial \chi^{HS}(\nu, T_0^{HS})}{\partial \nu} \right|_{\nu=20 \text{ keV}} = \left. \frac{\partial \chi(\nu, T_e^{EW})}{\partial \nu} \right|_{\nu=20 \text{ keV}}. \quad (6)$$

Equations (4) and (6), both being functions of only the peak hot-spot temperature, can be combined to form a scaling between a neutron-weighted and emissivity-weighted hot-spot temperature. This relationship has been calculated numerically for a range of relevant hot-spot temperatures and can be seen in Fig. 3(a) in blue, showing relatively higher emissivity-weighted temperatures at lower peak temperatures and higher neutron-weighted temperatures as the peak temperature is increased.

2D capsule simulations [17] were performed to examine the effects of more realistic implosion conditions including spatial asymmetries, time-dependent effects, and separate electron and ion temperatures. This simulation data set was

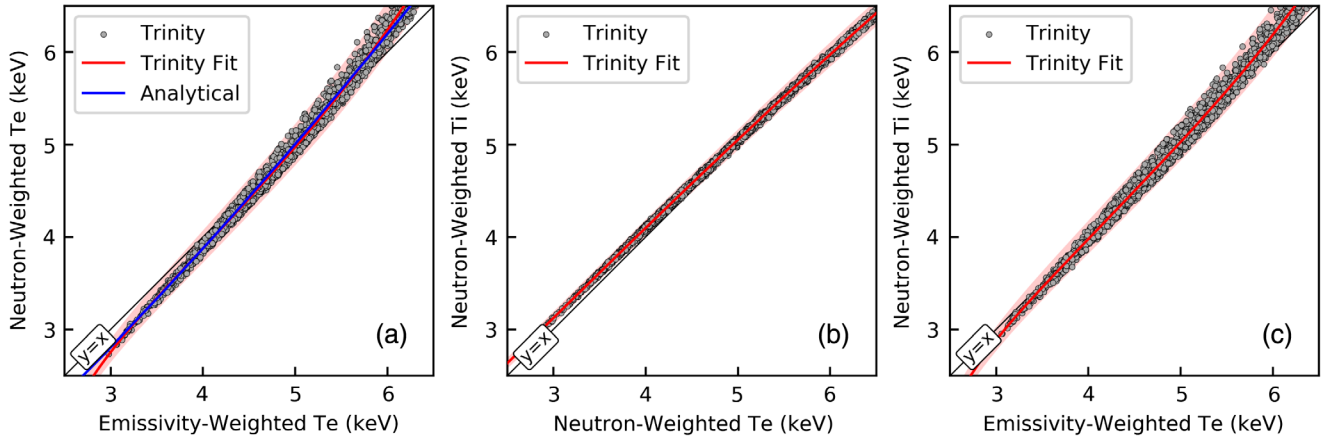


FIG. 3. Comparison of emissivity-weighted electron temperature, neutron-weighted electron temperature, and neutron-weighted ion temperature from simulation. (a) Neutron-weighted electron temperature plotted against emissivity-weighted electron temperature showing *weighting* differences of measurements. Red and blue lines correspond to fit to simulation database and analytic solution Eqs. (4) and (6). (b) Neutron-weighted ion temperature plotted against neutron-weighted electron temperature showing *species* temperature differences. (c) Neutron-weighted ion temperature plotted against emissivity-weighted electron temperature which is used to compare TiDFS measurements to NTOF measurements and extract RKE.

created using the Trinity Supercomputer at Los Alamos National Laboratory. Tens of thousands of 2D HYDRA capsule simulations were run covering a nine-dimensional parameter space including drive amplitude variations of $\pm 25\%$ and drive asymmetry variations including Legendre modes 1, 2, and 4 with respective variations of $\pm 2\%$, $\pm 10\%$, and $\pm 5\%$. The simulations were based on a high-density carbon ablator design [18–21]. In particular, these 2D simulations spanned hot-spot peak temperatures from ~ 3 to 9 keV, fuel areal densities from ~ 0.01 to 4 g/cm², hot-spot masses from 1 to 50 μg , and confinement times from ~ 70 to 130 ps.

With each simulation, the x-ray emission is extracted and used to infer a time-integrated electron temperature identically to the experimental data, while the time-integrated, neutron-weighted electron and ion temperatures from this data set are “born” values, unperturbed by potential down-scattering from the shell and bulk velocity motion. These three quantities are plotted against one another in Figs. 3(a)–3(c). In Fig. 3(a), the emissivity-weighted and neutron-weighted electron temperatures are plotted. With identical species, this relationship is structurally identical to the analytical relationship derived in Eqs. (4) and (6). As can be seen in Fig. 3(a), the polynomial fit to the simulation data set (red) matches the analytical model (blue), implying that a static isobaric model is a good approximation to full 2D implosions over a large range of implosion conditions. Plotted in Fig. 3(b) are neutron-weighted electron and ion temperatures which show good agreement to one another to within 4%. More specifically, at temperatures below 4 keV, where α -particle heating is minimal, the ion temperature is slightly higher, implying that shock heating is

contributing, percentagewise, more to the ions than electrons. As the temperature increases above 6 keV, the electron temperature begins to surpass the ion temperature due to preferential α -particle heating of electrons. In Fig. 3(c), the neutron-weighted ion temperature and emissivity-weighted electron temperature are plotted. Electron and ion temperatures are in good agreement within temperatures of interest to ICF (4–5 keV) and implicitly incorporate electron-ion temperature differences resulting from heating mechanisms such as shock heating and α -particle heating. The variance in ion and electron temperatures from this simulation data set, which includes severely perturbed drive asymmetries, is less than $\pm 3\%$.

Rather than directly comparing experimental ion temperature and x-ray electron temperature measurements, the *fit* to the simulated electron-ion temperature relationship can be used as a zero-RKE contour to more accurately understand temperature differences between the two measurements. This can be seen in Fig. 4, showing the measured ion and electron temperatures for a series of recent cryogenic DT implosion on the NIF, plotted with the zero-RKE contour fit from the simulation data set. In particular, the previously mentioned, high-hohlraum gas fill experiment can be seen in green, showing a systematic over-prediction in the ion temperature of ~ 800 eV, consistent with previous estimations [8] of the anomalously high DT ion temperature.

Using the measured difference in temperatures between the NTOF and TiDFS convolved with the simulated T_e/T_i scaling function, one can estimate the magnitude of burn-averaged residual kinetic energy, not converted to internal energy within the hot spot, for each implosion according to the following equations from Ref. [10]:

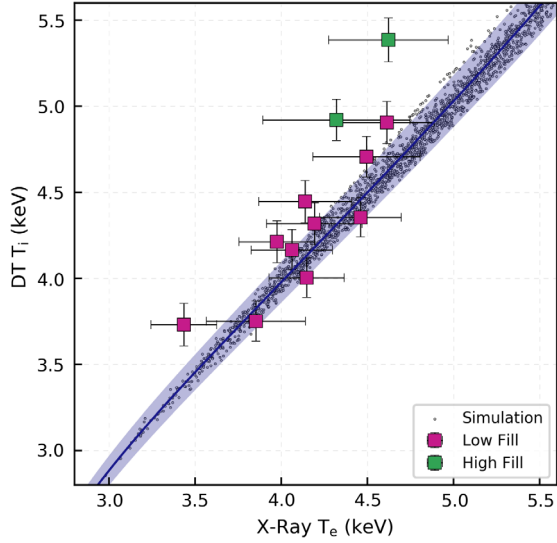


FIG. 4. Comparison of the emissivity-weighted electron temperature inferred from x-ray continuum measurements with neutron-weighted ion temperature measurements inferred from NTOF ion velocity variance measurements. A *zero-RKE* contour of the relation between the x-ray electron temperature and the neutron-weighted ion temperature is shown in dark blue to illustrate expected differences in T_i^{NW} and T_e^{EW} .

$$\sigma_v^2 = \frac{T_{\text{NTOF}}^{\text{NW}} - T_i^{\text{NW}}}{m_n + m_\alpha} = \frac{\Delta T_{\text{HS}}}{m_n + m_\alpha}, \quad (7)$$

$$\mathcal{E}_{\text{RKE}} = \frac{3}{2} \frac{M_{\text{HS}}}{m_n + m_\alpha} \Delta T_{\text{HS}}, \quad (8)$$

$$\mathcal{E}_T = 3 \frac{M_{\text{HS}}}{m_n + m_\alpha} T_{\text{HS}}, \quad (9)$$

where \mathcal{E}_{RKE} and \mathcal{E}_T are the hot-spot residual kinetic energy and internal energy, respectively. M_{HS} is the hot-spot mass, roughly estimated from the measured neutron yield, hot-spot volume, and burn duration [1]. In the case of the high gas fill hohlraum, with a temperature difference of 800 ± 260 eV, and hot-spot mass $M_{\text{HS}} = 15 \pm 5$ μg , we calculate a residual kinetic energy of 350 ± 150 J, or $\sim 9\%$ of the estimated internal energy within the hot spot. For the low gas fill hohlraum experiments, we calculate a mean temperature difference of 130 eV, corresponding to a residual kinetic energy of 50 ± 25 J, or $\sim 1\%$ of the hot-spot internal energy.

In summary, we have developed an electron temperature diagnostic on the NIF using titanium differential filters. This TiDFS measures temperature-dependent x rays produced within the hot spot with sufficient accuracy to use, in parallel and compared with, NTOF ion temperature measurements. Using the Trinity simulation database, we have developed a relationship between emissivity-weighted electron temperatures and neutron-weighted ion temperatures. In the specific case of high-foot repeat experiments, which used high

hohlraum gas fill, we see NTOF ion temperature measurements overpredicting the thermal temperature measurement, consistent with the presence of residual velocity flows broadening the neutron spectral measurements. In a more recent cryogenic implosion, which used a low hohlraum gas fill pressure, we see much smaller temperature differences, indicating more efficient conversion of shell kinetic energy to internal energy.

We thank the NIF operations team. This work was performed under the auspices of the U.S. Department of Energy by Lawrence Livermore National Laboratory under Contract No. DE-AC52-07NA27344.

*jarrott1@llnl.gov

- [1] O. A. Hurricane, D. A. Callahan, D. T. Casey, P. M. Celliers, C. Cerjan, E. L. Dewald, T. R. Dittrich, T. Döppner, D. E. Hinkel, L. F. B. Hopkins, J. L. Kline, S. Le Pape, T. Ma, A. G. MacPhee, J. L. Milovich, A. Pak, H. S. Park, P. K. Patel, B. A. Remington, J. D. Salmonson *et al.*, Fuel gain exceeding unity in an inertially confined fusion implosion, *Nature (London)* **506**, 343 (2014).
- [2] M. J. Edwards, J. D. Lindl, B. K. Spears, S. V. Weber, L. J. Atherton, D. L. Bleuel, D. K. Bradley, D. A. Callahan, C. J. Cerjan, D. Clark, G. W. Collins, J. E. Fair, R. J. Fortner, S. H. Glenzer, S. W. Haan, B. A. Hammel, A. V. Hamza, S. P. Hatchett, N. Izumi, B. Jacoby *et al.*, The experimental plan for cryogenic layered target implosions on the National Ignition Facility—The inertial confinement approach to fusion, *Phys. Plasmas* **18**, 051003 (2011).
- [3] J. D. Lindl, P. Amendt, R. L. Berger, S. G. Glendinning, S. H. Glenzer, S. W. Haan, R. L. Kauffman, O. L. Landen, and L. J. Suter, The physics basis for ignition using indirect-drive targets on the National Ignition Facility, *Phys. Plasmas* **11**, 339 (2004).
- [4] O. A. Hurricane, D. A. Callahan, D. T. Casey, E. L. Dewald, T. R. Dittrich, T. Döppner, M. A. Barrios Garcia, D. E. Hinkel, L. F. B. Hopkins, P. Kervin, J. L. Kline, S. L. Pape, T. Ma, A. G. MacPhee, J. L. Milovich, J. Moody, A. E. Pak, P. K. Patel, H. S. Park, B. A. Remington *et al.*, The high-foot implosion campaign on the National Ignition Facility, *Phys. Plasmas* **21**, 056314 (2014).
- [5] H.-S. Park *et al.*, High-Adiabatic High-Foot Inertial Confinement Fusion Implosion Experiments on the National Ignition Facility, *Phys. Rev. Lett.* **112**, 055001 (2014).
- [6] R. Betti, P. Y. Chang, B. K. Spears, K. S. Anderson, J. Edwards, M. Fatenejad, J. D. Lindl, R. L. McCrory, R. Nora, and D. Shvarts, Thermonuclear ignition in inertial confinement fusion and comparison with magnetic confinement, *Phys. Plasmas* **17**, 058102 (2010).
- [7] R. Betti, A. R. Christopherson, B. K. Spears, R. Nora, A. Bose, J. Howard, K. M. Woo, M. J. Edwards, and J. Sanz, Alpha Heating and Burning Plasmas in Inertial Confinement Fusion, *Phys. Rev. Lett.* **114**, 255003 (2015).
- [8] O. A. Hurricane, D. A. Callahan, D. T. Casey, E. L. Dewald, T. R. Dittrich, T. Döppner, S. Haan, D. E. Hinkel, L. F. B. Hopkins, O. Jones, A. L. Kritcher, S. Le Pape, T. Ma, A. G. MacPhee, J. L. Milovich, J. Moody, A. Pak, H. S. Park,

- P. K. Patel, J. E. Ralph *et al.*, Inertially confined fusion plasmas dominated by alpha-particle self-heating, *Nat. Phys.* **12**, 800 (2016).
- [9] M. G. Johnson, J. P. Knauer, C. J. Cerjan, M. J. Eckart, G. P. Grim, E. P. Hartouni, R. Hatarik, J. D. Kilkenny, D. H. Munro, D. B. Sayre, B. K. Spears, R. M. Bionta, E. J. Bond, J. A. Caggiano, D. Callahan, D. T. Casey, T. Döppner, J. A. Frenje, V. Y. Glebov, O. Hurricane *et al.*, Indications of flow near maximum compression in layered deuterium-tritium implosions at the National Ignition Facility, *Phys. Rev. E* **94**, 021202(R) (2016).
- [10] T. J. Murphy, The effect of turbulent kinetic energy on inferred ion temperature from neutron spectra, *Phys. Plasmas* **21**, 072701 (2014).
- [11] A. L. Kritcher, R. Town, D. Bradley, D. Clark, B. Spears, O. Jones, S. Haan, P. T. Springer, J. Lindl, R. H. H. Scott, D. Callahan, M. J. Edwards, and O. L. Landen, Metrics for long wavelength asymmetries in inertial confinement fusion implosions on the National Ignition Facility, *Phys. Plasmas* **21**, 042708 (2014).
- [12] D. S. Clark, C. R. Weber, J. L. Milovich, J. D. Salmonson, A. L. Kritcher, S. W. Haan, B. A. Hammel, D. E. Hinkel, O. A. Hurricane, O. S. Jones, M. M. Marinak, P. K. Patel, H. F. Robey, S. M. Sepke, and M. J. Edwards, Three-dimensional simulations of low foot and high foot implosion experiments on the National Ignition Facility, *Phys. Plasmas* **23**, 056302 (2016).
- [13] A. Inglebert, B. Canaud, and O. Larroche, Species separation and modification of neutron diagnostics in inertial-confinement fusion, *Europhys. Lett.* **107**, 65003 (2014).
- [14] N. Izumi, J. Lee, E. Romano, G. Stone, B. Maddox, T. Ma, V. Rekow, D. K. Bradley, and P. Bell, in *SPIE Optical Engineering + Applications*, edited by P. M. Bell and G. P. Grim (SPIE, Bellingham, WA, 2013), pp. 885006–8, DOI: [10.1117/12.2024513](https://doi.org/10.1117/12.2024513).
- [15] L. C. Jarrott, L. R. Benedetti, H. Chen, N. Izumi, S. F. Khan, T. Ma, S. R. Nagel, O. L. Landen, A. Pak, P. K. Patel, M. Schneider, and H. A. Scott, Scan-dependent image plate response function for high dynamic range x-ray experiments (to be published).
- [16] L. C. Jarrott, L. R. Benedetti, H. Chen, N. Izumi, S. F. Khan, T. Ma, S. R. Nagel, O. L. Landen, A. Pak, P. K. Patel, M. Schneider, and H. A. Scott, Hotspot electron temperature from x-ray continuum measurements on the NIF, *Rev. Sci. Instrum.* **87**, 11E534 (2016).
- [17] J. L. Peterson, K. D. Humbird, J. E. Field, S. T. Brandon, S. H. Langer, R. C. Nora, B. K. Spears, and P. T. Springer, Zonal flow generation in inertial confinement fusion implosions, *Phys. Plasmas* **24**, 032702 (2017).
- [18] L. F. B. Hopkins, N. B. Meezan, S. Le Pape, L. Divol, A. J. Mackinnon, D. D. Ho, M. Hohenberger, O. S. Jones, G. Kyrala, J. L. Milovich, A. Pak, J. E. Ralph, J. S. Ross, L. R. Benedetti, J. Biener, R. Bionta, E. Bond, D. Bradley, J. Caggiano, D. Callahan *et al.*, First High-Convergence Cryogenic Implosion in a Near-Vacuum Hohlraum, *Phys. Rev. Lett.* **114**, 175001 (2015).
- [19] L. F. B. Hopkins, S. Le Pape, L. Divol, N. B. Meezan, A. J. Mackinnon, D. D. Ho, O. S. Jones, S. Khan, J. L. Milovich, J. S. Ross, P. Amendt, D. Casey, P. M. Celliers, A. Pak, J. L. Peterson, J. Ralph, and J. R. Rygg, Near-vacuum hohlraums for driving fusion implosions with high density carbon ablaters), *Phys. Plasmas* **22**, 056318 (2015).
- [20] A. J. Mackinnon, N. B. Meezan, J. S. Ross, S. Le Pape, L. F. B. Hopkins, L. Divol, D. Ho, J. Milovich, A. Pak, J. Ralph, T. Döppner, P. K. Patel, C. Thomas, R. Tommasini, S. Haan, A. G. MacPhee, J. McNaney, J. Caggiano, R. Hatarik, R. Bionta *et al.*, High-density carbon ablator experiments on the National Ignition Facility, *Phys. Plasmas* **21**, 056318 (2014).
- [21] L. Divol, A. Pak, L. F. B. Hopkins, S. L. Pape, N. B. Meezan, E. L. Dewald, D. D. M. Ho, S. F. Khan, A. J. Mackinnon, J. S. Ross, D. P. Turnbull, C. Weber, P. M. Celliers, M. Millot, L. R. Benedetti, J. E. Field, N. Izumi, G. A. Kyrala, T. Ma, S. R. Nagel, Symmetry control of an indirectly driven high-density-carbon implosion at high convergence and high velocity, *Phys. Plasmas* **24**, 056309 (2017).